



Three-dimensional reconstruction of wear particle surface based on photometric stereo

Shuo Wang^{a,b}, Tonghai Wu^{a,b,*}, Lingfeng Yang^{a,b}, Ngaiming Kwok^c, Thompson Sarkodie-Gyan^d

^a Xi'an Jiaotong University, School of Mechanical Engineering, Xi'an, Shaanxi 710049, PR China

^b Xi'an Jiaotong University, Key Laboratory of Education Ministry for Modern Design and Rotor-Bearing System, Xi'an, Shaanxi 710049, PR China

^c The University of New South Wales, School of Mechanical and Manufacturing Engineering, Sydney 2052, Australia

^d University of Texas at El Paso, Department of Electrical and Computer Engineering, Laboratory for Industrial Metrology and Automation, El Paso, USA

ARTICLE INFO

Article history:

Received 6 July 2018

Received in revised form 10 October 2018

Accepted 11 October 2018

Available online 12 October 2018

Keywords:

Ferrography

Wear particle analysis

Photometric stereo

Three-dimensional reconstruction

ABSTRACT

Ferrography has emerged as a significant candidate for the provision of relevant information for the determination of the status of machine wear. However, this conventional methodology provides only marginal results due to its inability to provide 3-dimensional (3D) surface information. The authors of this paper have developed a methodology based on photometric-stereo towards the enhancement of the capabilities of ferrography. This enhanced and innovative methodology consists of three main components, the multi-illumination image acquisition, the wear particle extraction, and the 3D surface reconstruction. The methodology ensures the reliable and efficient extraction of the wear particles surface topographies for further feature-based wear particle identification. The performance of this methodology has been compared with results observed from the laser scanning confocal microscopy. The outcome of this comparison has depicted that the methodology involving this new low-cost ferrography system exhibits very high accuracy for the 3D surface feature extraction of wear particles.

© 2018 Elsevier Ltd. All rights reserved.

1. Introduction

Wear particles bear very significant information inherent in the determination of wear severity and wear mechanisms, whereby, the wear particles result from the direct production of friction interactions between mechanical parts [1]. WDA may be accounted for as a significant means for machine condition monitoring [2–4]. These methods have been extensively explored and implemented focusing on particle morphological characteristics, and there is a continuous improvement in the various methodologies towards effectiveness.

Ferrography has emerged as one of the most recognized and effective WDA methods in recent years [5]. In fact, it has been widely used in industrial machines including the monitoring of marine and aircraft engines [6–8]. Due to the ferromagnetic properties of wear particles, this methodology takes advantage of a high gradient magnetic field for the collection of wear particles emanating from the lubrication oil. An optical microscope is then applied to capture the particle images. The application of image processing enables the acquisition and analysis of wear particle shapes, texture and material characteristics as inference parameters for wear mechanisms [9].

* Corresponding author at: Xi'an Jiaotong University, School of Mechanical Engineering, Xi'an, Shaanxi 710049, PR China.

E-mail address: wt-h@163.com (T. Wu).

The current acquisition and processing methods only provide 2D characteristics of the image rather than spatial features. The absence of spatial features offers only marginal results since there is no reflection whatsoever of the real shapes of the irregular wear particles including the laminar, adhesive and severe sliding particles [10]. Whereas both laminar and severe sliding particles exhibit similar shapes and edge features in 2D images, laminar particles exhibit holes, wrinkles and other surface defects in 3D images. In fact, severe sliding particles exhibit parallel slips or cracks on the surfaces, therefore, there arises the requirement for additional dimensions to enable further identification of the unobservable types of wear particles.

The electron microscopy has enhanced research activities towards the extraction of particle features in 3D. Some examples of the enhancements for the provision of information with respect to the wear debris contours and surfaces include AFM [11,12], LSCM [13], and SEM [14], respectively. The analysis and comparison of results clearly depict reliability and efficiency in the performance of the 3D wear particles method over the 2D one. In spite of this distinction, the application of this 3D methodology is still marginalized due to its high costs and complex operation. Several factors seem to impose restrictions on the application of the electron microscope in WDA. As an example, the measurement range

Nomenclature

Items	Definition		
s	scale factor	$D_i(x, y)$	the image handled by the difference method
m'	the 2D coordinates of the image	$f_i(x, y)$	the image of the i -th IS
K	camera intrinsic matrix	$f_0(x, y)$	the mask image
R	rotation matrix	ρ	the reflection coefficient of the object surface
t	translation matrix	N_0	the unit normal vector on the WPS
M	3D coordinate in space	L_0	the IS direction
u_0	the x-coordinate of the pivot points	3D	3-dimensinal
v_0	the y-coordinate of the pivot points	2D	2-dimensinal
f_u	the focal lengths of the camera on the u -axis	WDA	Wear Debris Analysis
f_v	the focal lengths of the camera on the v -axis	AFM	atomic force microscope
(u, v)	real pixel coordinates	LSCM	the laser scanning confocal microscopy
(\bar{u}, \bar{v})	ideal pixel coordinates	SEM	stereo scanning electron microscopy
(x, y)	the real image coordinates	PS	photometric stereo
(\bar{x}, \bar{y})	the ideal image coordinates	OTSU	maximum between-class variance method
k_1	second-order radial distortion coefficients	WPS	wear particle surface
k_2	fourth-order radial distortion coefficients	MII	multi-illumination image
ω_0	the proportion of the foreground	RWPS	reconstruction of wear particle surface
μ_0	average gray level of foregrounds	IS	illumination source
ω_1	the proportion of the background	ITM	the iterative threshold method
μ_1	the average gray level of background	MESM	by the maximum entropy segmentation method

of the AFM is confined to wear particle sizes below 5 μm in which case it may be deemed as insignificant for any practical engineering applications. The LSCM is more frequently applied in the examination of biological particles as opposed to particles from mechanical parts. In addition to these restrictions is the fact that these methods largely focus on the analysis of a single wear particle, but not simultaneously on the multiple particle morphologies.

As a contribution towards the further enhancement of the aforementioned issues, it becomes very necessary to develop other effective WDA methods. One of such possibilities is the 3D RWPS based on 2D image sequences [15]. The principles underlying these video based techniques are very similar, and they function as follows: wear particles are rolled into a free-flow channel whereby a camera is mounted on the microscope for capturing the video images of the particles in the flowing lubricant. A scheme that is similar to this method is reported for the estimation of 3D particle information in reference [16], which extends WDA from 2D to 3D. In fact, the resulting 3D model does not represent a comprehensive reflection of the particle since only two images may be under consideration. There follows a further improvement of this approach through the extraction of 2D features from multiple views for the construction of 3D features [17]. Furthermore, the 3D model of the particles is constructed based on a silhouette-based method from full-view images [18]. However, 3D surface morphology of wear particles may not be observed through these methods.

Although current WDA methodologies have gained some successes in machine condition monitoring, yet still, they are insufficient in the acquisition of comprehensive, reliable and accurate wear information. This paper introduces a new 3D reconstruction ferrography system based on photometric stereo for the analysis of WPSs. Wear particles from lubricants are acquired using procedures of ferrography. An optical microscope is then applied for the acquisition of the particle images under multiple ISs located at specifically selected positions. This proposed method consists of four main stages; (1) an image acquisition system consisting of an optical microscope and eight- ISs, (2) a processing arrangement for the enhancement of image degradations due to possible lens distortions, (3) the extraction of the wear particles using the OTSU and differencing methods, and (4) the reconstruction of the WPSs

using the surface normal and height calculations. Finally, there follow a comparison of the reconstructed surfaces with those from the LSCM.

This paper is further organized as follows: Section 2 is the description of the procedure involving the acquisition of multi-illumination particle image, the wear particle extraction, and the 3D RWPSs with photometric stereo; the verification of the proposed method is given in Section 3; discussions are presented in Section 4; and conclusions are depicted in Section 5.

2. Materials and methods

PS technology is a significant methodology that enables the estimation of the surface normal from the captured MIIs for the reconstruction of the surface [19]. In view of the particularity of wear particles, a 3D Reconstruction of WPS method based on PS is developed in this section that consists of three steps; (1) Image acquisition from multiple ISs, (2) Wear particle extraction, and (3) 3D Reconstruction of WPS.

2.1. Image acquisition from multiple ISs

Considering the small size of wear particles, it becomes very difficult to obtain multiple ISs using only traditional camera phenomena. Therefore, an additional optical microscope is included in the optical path to enhance the capture capabilities of images of the wear particles under multiple ISs. The subsequent processing procedures involving the estimation of the direction of the incidence illumination and the rectification of the distorted images are further described below.

2.1.1. Wear particle image acquisition system

PS technology recovers WPSs from MIIs taken from the same view. It follows the assumption that ISs are sufficiently so far away from the object such that all incidence ISs may be considered as parallel rays with equal intensity, as shown in Fig. 1 (a) and (b). Hence, a PS system is designed consisting of an optical microscope and eight LEDs, as shown in Fig. 1 (c). The distance between the IS

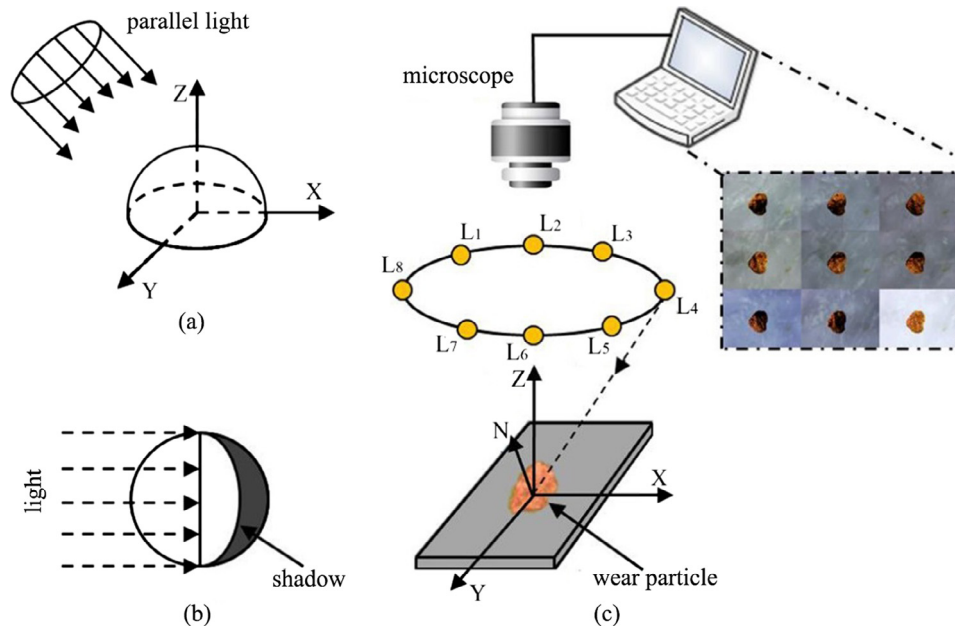


Fig. 1. Diagram of the 3D RWPS: (a) object illuminated by parallel rays; (b) surface shadows; (c) acquisition system for MILs.

and the wear particles should exceed 40 mm. Furthermore, it may be considered that the LEDs are located at infinity such that their incidence illuminations are in parallel to the wear particles since the wear particle sizes are, generally, less than 200 μm . In order to collect real MILs of wear particles, white illumination sources are introduced into the wear particle image acquisition system. The luminous intensity (IV) ranging between 9000 mcd and 14,000 mcd enables the illumination source to light up wear particles, but will not generate any specular reflections on WPSs. The LED specifications are given in Table 1.

Wear particle samples, collected by ferrography, are placed under the microscope. When the eight LEDs are sequentially powered on and off, MILs are captured by the microscope-camera arrangement. Additionally, a fully illuminated wear particle image is captured when the eight LEDs are simultaneously powered on. The acquired images are shown in Fig. 2. As may be observed from Fig. 2 (a) ~ (h), the shadow on the WPS rotates with the eight LEDs powered on and off which clearly illustrates the effectiveness of the designed PS system.

2.1.2. Illumination direction estimation

The perception of an object depends on its geometric and brightness variations on the surface. In addition, a significant factor for brightness variations is the direction of the incidence illumination. This factor has a direct influence on the computation of the normal vector of the surface, hence, the necessity for an appropriate procedure in the estimation of the direction of the illumination [20].

Traditional methods estimate the directions of the incidence illumination with reference to known geometric or spatial posi-

tions. Image features, e.g. specular points, are estimated when the IS strikes on the object surface [21]. Alternatively, the directions of the incidence illumination may be deduced by normalizing the actual distances between the ISs and the wear particles. Due to the very small distance (negligible) between the particle and the microscope for referencing the indicators, the latter method is applied in the system and the estimation results are then illustrated in Table 2.

2.1.3. Distorted image rectification

The real camera lens is, generally, incapable of satisfying the strictly essential center projection relationship required by the pin-hole imaging principle. Based on this shortcoming, there arise distortions in the captured images. It becomes then necessary to rectify the original images through the estimated parameters of the camera for further processing. From reference [22], it is required to move either the camera or the plane checkerboard to various positions in space, and then capture the images of the plane checkerboard.

(a) Camera intrinsic matrix

In order to solve the problem involving distortion coefficients, there is the initial requirement to calibrate the intrinsic matrix of the microscope-camera arrangement. Within the context of image processing as in reference [23], a point in space maps to pixels in the image and this relationship may be expressed in Eq. (1) as:

$$sm' = KR^{-1}[I - t]M = \begin{bmatrix} f_u & 0 & u_0 \\ 0 & f_v & v_0 \\ 0 & 0 & 1 \end{bmatrix} R^{-1}[I - t]M = HM \quad (1)$$

where s is the scale factor, m' is the 2D coordinates of the image, K is the camera intrinsic matrix, R is the rotation matrix, t is the translation matrix, M is the 3D coordinate in space, $H = [h_1, h_2, h_3]$, u_0 and v_0 are the coordinates of the pivot points (the intersection point of the optical axis with the imaging plane), f_u and f_v are the focal lengths of the camera on the u -axis and v -axis, respectively.

From Eq. (1), the constraints of the intrinsic matrix parameters may be solved as in Eqs. (2) and (3) as,

Table 1
LED specification.

Indicator	Parameters
IV(mcd)	9000–14,000
CCT(K)	X:0.2890–0.3168/Y:0.3008–0.3203
VF(V)	2.8–3.0
Colors	white

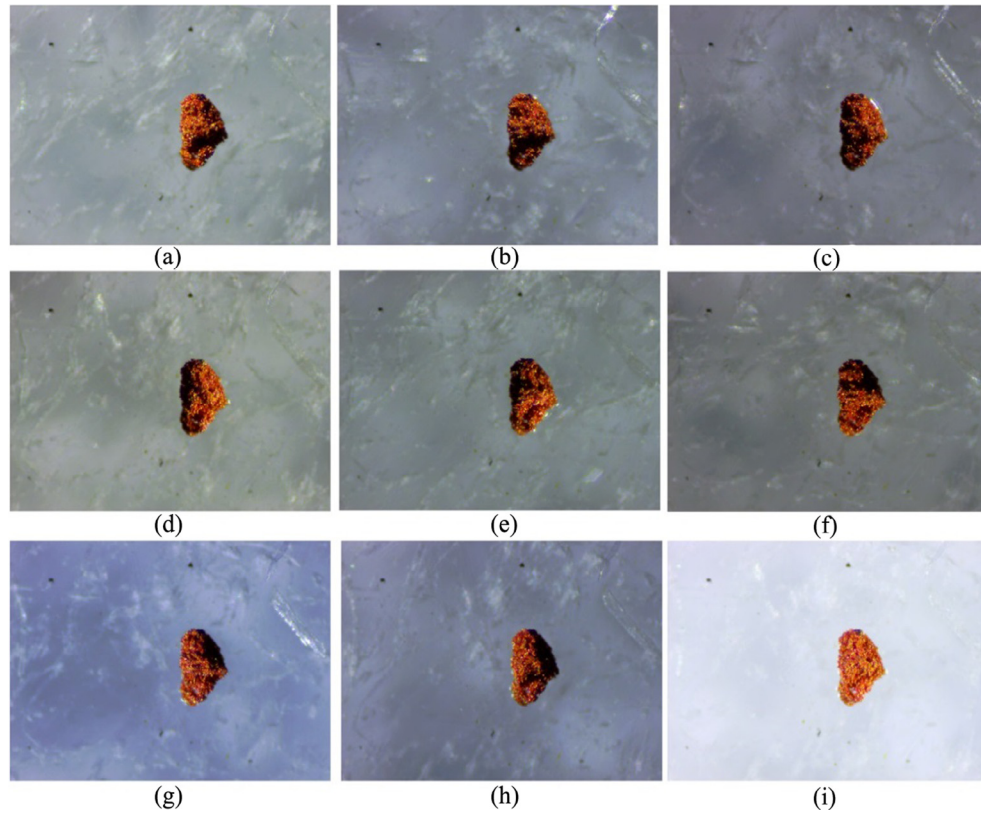


Fig. 2. Wear particle images captured from multiple ISs: (a) wear particles captured under L_1 ; (b) wear particles captured under L_2 ; (c) wear particles captured under L_3 ; (d) wear particles captured under L_4 ; (e) wear particles captured under L_5 ; (f) wear particles captured under L_6 ; (g) wear particles captured under L_7 ; (h) wear particles captured under L_8 ; (i) the fully illuminated wear particles image.

Table 2
Incidence illumination direction estimation results.

LED	Real distance (x, y, z)	Incidence illumination direction ($\bar{x}, \bar{y}, \bar{z}$)
L_1	(−29.7, 29.7, 33)	(−0.56, 0.56, 0.62)
L_2	(0, 42, 33)	(0, 0.79, 0.62)
L_3	(29.7, 29.7, 33)	(0.56, 0.56, 0.62)
L_4	(42, 0, 33)	(0.79, 0, 0.62)
L_5	(29.7, −29.7, 33)	(0.56, −0.56, 0.62)
L_6	(0, −42, 33)	(0, −0.79, 0.62)
L_7	(−29.7, −29.7, 33)	(−0.56, −0.56, 0.62)
L_8	(−42, 0, 33)	(−0.79, 0, 0.62)

$$h_1^T K^{-T} K^{-1} h_2 = 0 \quad (2)$$

$$h_1^T K^{-T} K^{-1} h_1 = h_2^T K^{-T} K^{-1} h_2 \quad (3)$$

These two constraint equations are derived from one image. Thus, the four parameters (f_u, f_v, u_0 and v_0) in the intrinsic matrix may be derived only from two images. To facilitate an improvement in the calibration accuracy, eight images of plane checkerboard are acquired through the variation of the relative positions between camera and checkerboard, as in Fig. 3. Every checkerboard image has 20 corner points, and these corners are extracted by using the Harris method [24]. The extracted corner positions are fed into Eqs. (2) and (3), so that the camera intrinsic matrix can be estimated as:

$$K = \begin{bmatrix} 34043.51 & 0 & 863.53 \\ 0 & 33376.80 & 430.49 \\ 0 & 0 & 1 \end{bmatrix} \quad (4)$$

(b) Radial distortion coefficient

Radial distortions are always inherent in images. Based on this hypothesis, the distortion center is always considered as the main point of the camera, in which the distortion is similar in both the x -axis and y -axis, respectively. A combination of the camera internal reference model may be expressed as $\bar{u} = u_0 + x/dx$ and $\bar{v} = v_0 + y/dy$, the mathematical model of the radial distortion may be expressed as,

$$\begin{cases} u = \bar{u} + (\bar{u} - u_0) \left[k_1 (\bar{x}^2 + \bar{y}^2) + k_2 (\bar{x}^2 + \bar{y}^2)^2 \right] \\ v = \bar{v} + (\bar{v} - v_0) \left[k_1 (\bar{x}^2 + \bar{y}^2) + k_2 (\bar{x}^2 + \bar{y}^2)^2 \right] \end{cases} \quad (5)$$

where (u, v) are the real pixel coordinates, (\bar{u}, \bar{v}) are the ideal pixel coordinates, (x, y) are the real image coordinates, (\bar{x}, \bar{y}) are the ideal image coordinates, and k_1, k_2 are second-order and fourth-order radial distortion coefficients, respectively.

In Part a), the corner point coordinates in the checkerboard images were extracted. From Eq. (5), the radial distortion coefficients were obtained with application of the least square method as; $k_1 = -7.73$ and $k_2 = -0.15$. In addition, the MIs of wear particles were corrected by the radial distortion coefficients as illustrated in Fig. 4 (b). For comparison with the original images, the corrected pixel images are made to become smaller towards the center of the image such that the closer the distances between the edges of the pixels and the images, the larger the scale of the reduction.

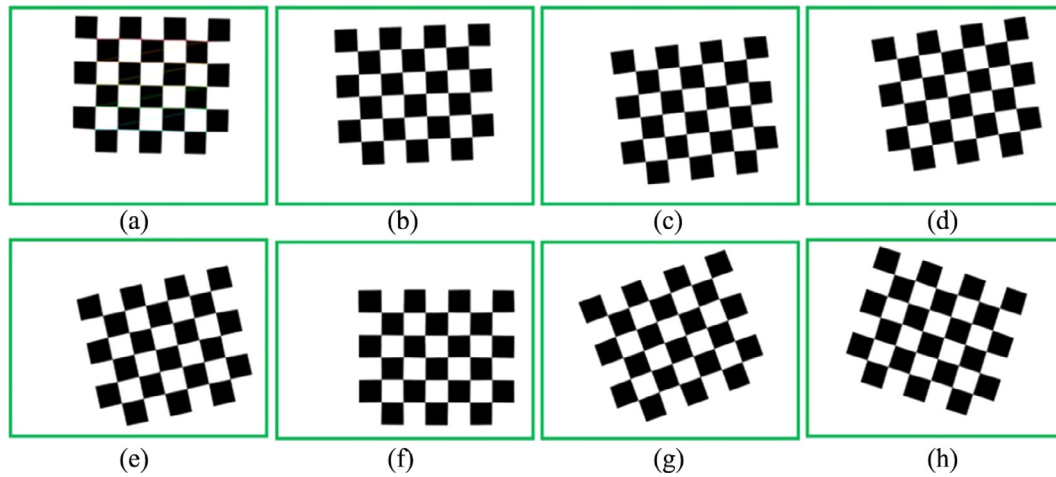


Fig. 3. Plane checkerboard images: (a) checkerboard captured at Position 1; (b) checkerboard captured at Position 2; (c) checkerboard captured at Position 3; (d) checkerboard captured at Position 4; (e) checkerboard captured at Position 5; (f) checkerboard captured at Position 6; (g) checkerboard captured at Position 7; (h) checkerboard captured at Position 8.

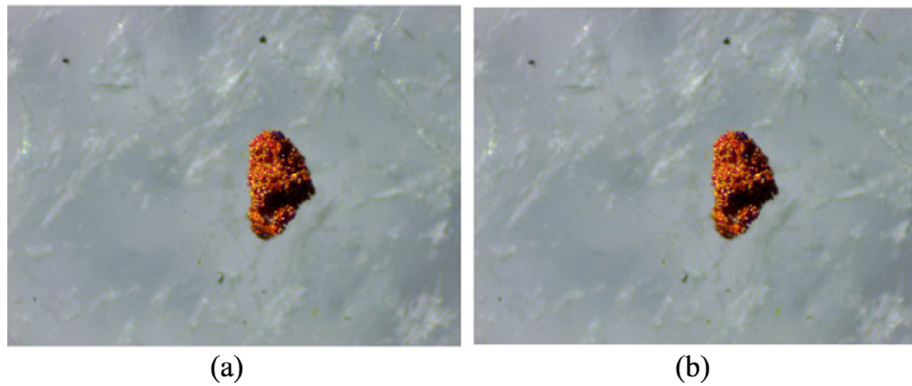


Fig. 4. Wear particle image rectification on Fig. 2 (a): (a) original wear particle image; (b) corrected wear particle images.

2.2. Wear particle extraction

The numerical increase in MIs makes reconstruction precision more ideal, and this will lead to a multiplicity of computational intensity. This problem would require the extraction of wear particles from the background region in order to improve the efficiency of the reconstruction method. Therefore, an adaptive extraction method is developed in this part that consists of two steps; (1) the mask image acquisition by OTSU, and (2) the wear particle extraction by the difference method, respectively.

2.2.1. Mask image acquisition by OTSU

There are very distinct differences between the wear particles and the background of the full-illumination image. The wear particles may be separable from the background with an appropriate threshold. Based on the gray-level properties of the wear particle images, OTSU provides a self-adaptive threshold for segmentation of the image into two categories. Should the result of the probability of the segmentation error be least indicates that the variance in the two categories is very large [25]. This result enables the adoption of the OTSU method whose basic principle is described as follows.

For a gray image, it can be assumed that the number of pixels in the image is N , the gray level changes from 0 to $l-1$, and the pixel number of the i -th gray level is n_i . By selecting an initial threshold k from the gray level, the wear particle image may be segmented

into two categories; foreground C_0 and background C_1 , where $C_0 = \{0, 1, 2, \dots, k\}$, and $C_1 = \{k+1, \dots, l-1\}$. Furthermore, the proportion of the foreground (ω_0), the average gray level of foregrounds (μ_0), the proportion of the background (ω_1) and the average gray level of background (μ_1) may be calculated as in Eq. (6). And the class variance between C_0 and C_1 may be defined as in Eq. (7) as,

$$\begin{cases} \omega_0 = \sum_{i=0}^k \frac{n_i}{N} & \mu_0 = \sum_{i=0}^k \frac{i \cdot n_i}{\omega_0 \cdot N} \\ \omega_1 = \sum_{i=k+1}^{l-1} \frac{n_i}{N} & \mu_1 = \sum_{i=k+1}^{l-1} \frac{i \cdot n_i}{\omega_1 \cdot N} \end{cases} \quad (6)$$

$$\sigma^2(k) = \omega_0 \omega_1 (\mu_0 - \mu_1)^2 \quad (7)$$

Variance reflects the range scope of data, thus, the greater the variance, the greater the difference between the two classes. By changing the threshold k from 0 to $l-1$, the optimal threshold k^* may be determined when $\sigma^2(k)$ is the largest quantity. Based on the obtained threshold k^* , the full-illumination image is segmented into binary images in which the wear particles are white areas and the black areas depict the background as in Fig. 5 (c). However, there appears the existence of several holes in the segmentation results due to the inhomogeneity of gray level on WPSs. In order to eliminate the noise, advantage is taken of the expansion and corrosion algorithm to fill these holes and, hence, the final segmentation results are shown as in Fig. 5 (d).

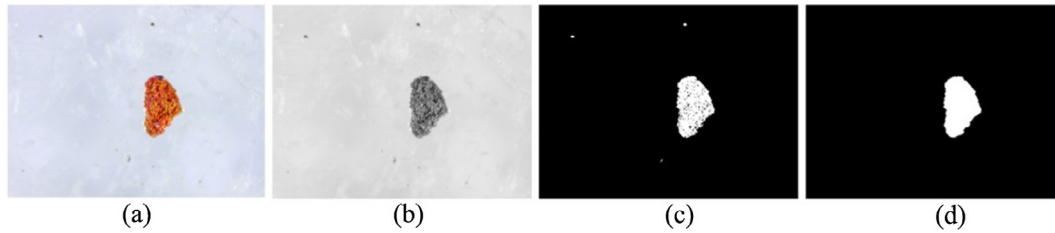


Fig. 5. The OTSU-based mask image acquisition method: (a) original image; (b) gray image; (c) segmentation results; (d) wear particle image with noise elimination.

To verify the performance of the OTSU-based mask image acquisition method, a set of experiments were performed by comparing the segmentation results with the results of the ITM [29] and the MESM [30,31]. The segmentation results are illustrated in Fig. 6. As may be observed, the particle images appear to exhibit some level of over-segmentation through the ITM, and there is much noise on the segmented image by virtue of the MESM. This leads to a failure towards obtaining complete wear particles. However, the OTSU-based mask image acquisition method is able to effectively extract wear particles and eliminate noises through a combination of the expansion and corrosion algorithms.

2.2.2. Wear particle extraction by differencing

After the acquisition of the mask images, the difference method, described in Eq. (8), is applied onto MILs in order to extract wear particles from the background, as depicted in Fig. 7.

$$D_i(x,y) = \begin{cases} f_i(x,y) & f_0(x,y) > 0 \\ 0 & f_0(x,y) = 0 \end{cases} \quad (8)$$

where $D_i(x,y)$ represents the image handled by the difference method, $f_i(x,y)$ represents the image of the i -th IS, and $f_0(x,y)$ represents the mask image.

2.3. 3D reconstruction of WPS

The brightness of MILs contains rich 3D information such as the relative height. Based on the extracted wear particle images, 3D surfaces of wear particle are reconstructed by PS [26,27]. The height of WPSs may be recovered by calculating the surface normal vectors from the multiple illumination image sources. Generally, there are two steps involved in this PS procedure; (1) the surface normal vector calculation, and (2) the surface height restoration, respectively. The first step is presented in Section 2.3.1 and the height solution process will be given in Section 2.3.2.

2.3.1. Surface normal vector calculation

The theory of optics suggests that when incidence illuminations strike on the object surface, they are reflected and transmitted based on the optical properties of the surface. However, part of this incidence illumination may be absorbed by the surface and converted into heat. The color of the object surface may only be estimated through the reflected illumination when the object is not transparent. With many protrusions on the surface, wear particle may reflect the illumination in all directions. Thus, it may be considered that the reflection on WPS is caused by the scattered

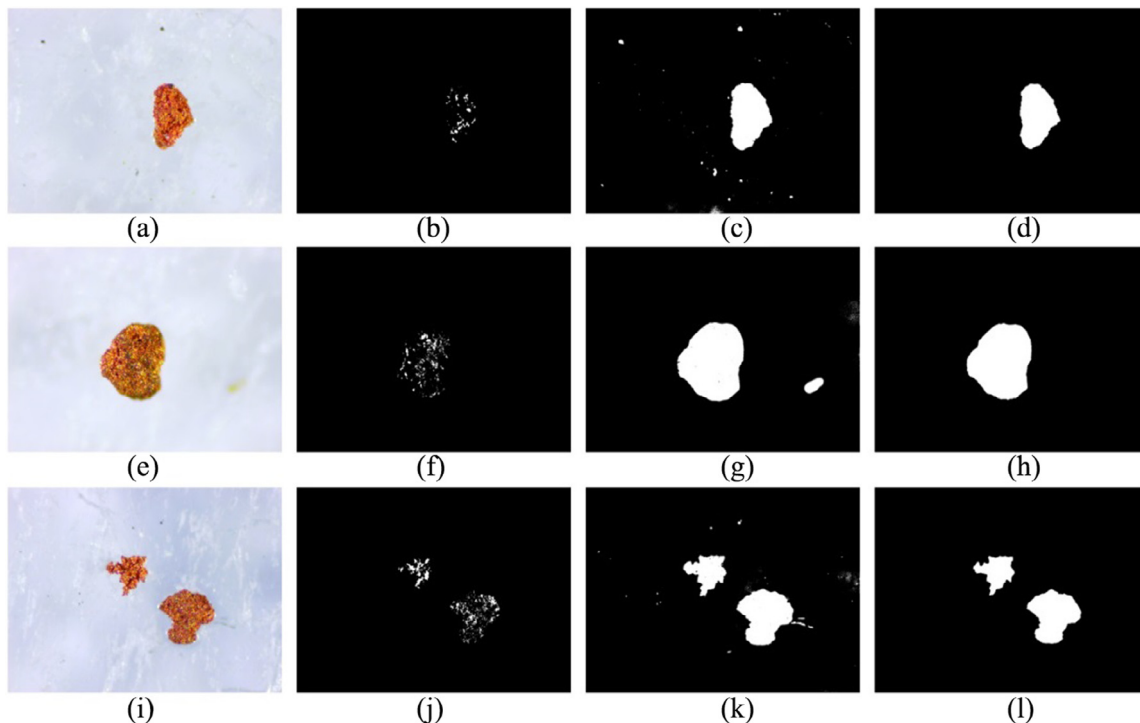


Fig. 6. Comparison of wear particles segmentation results: (a) particle image #1; (b) image #1 segmentation by the ITM; (c) image #1 segmentation by the MESM; (d) image #1 segmentation by the OTSU-based method; (e) particle image #2; (f) image #2 segmentation by the ITM; (g) image #2 segmentation by the MESM; (h) image #2 segmentation by the OTSU-based method; (i) particle image #3; (j) image #3 segmentation by the ITM; (k) image #3 segmentation by the MESM; (l) image #3 segmentation by the OTSU-based method.

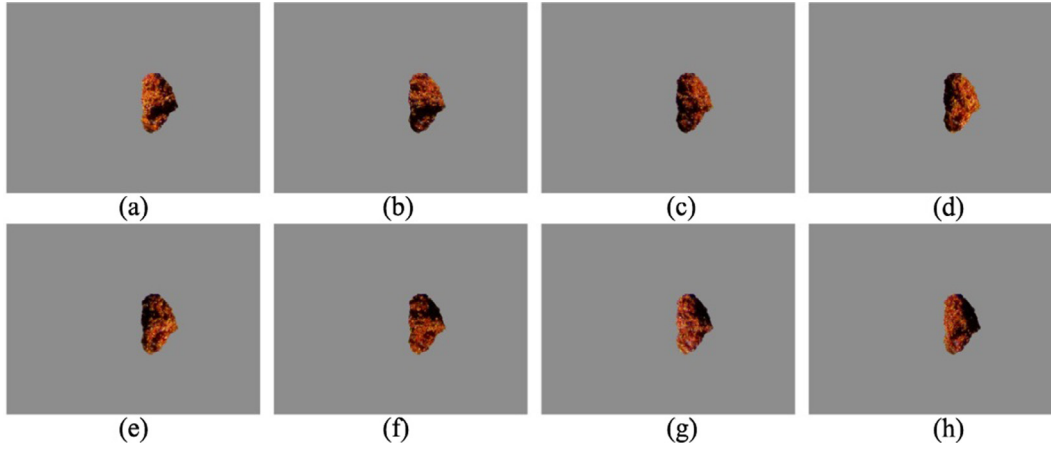


Fig. 7. Wear particles extraction: (a) wear particles extracted from L_1 image; (b) wear particles extracted from L_2 image; (c) wear particles extracted from L_3 image; (d) wear particles extracted from L_4 image; (e) wear particles extracted from L_5 image; (f) wear particles extracted from L_6 image; (g) wear particles extracted from L_7 image; (h) wear particles extracted from L_8 image.

illumination, which may be regarded as the Lambertian reflection model [19]. According to this model, the brightness I_0 on the image is expressed as:

$$I_0 = \rho N_0 \cdot L_0 \quad (9)$$

where ρ is the reflection coefficient of the object surface, N_0 represents the unit normal vector on the WPS, $N_0 = (N_x, N_y, N_z)^T$, L_0 represents the IS direction, $L_0 = (L_x, L_y, L_z)^T$.

It may be observed that Eq. (9) is a linear equation about each component of N . If the number of the equations is above three, the normal vector N could be determined. That is, the surface normal vector N may be computed with three or more captured images under different illumination conditions. Furthermore, eight wear particle images are acquired under different LEDs. Thus, Eq. (9) is extended as:

$$\begin{cases} I_1 = \rho(N_x \cdot L_{1x} + N_y \cdot L_{1y} + N_z \cdot L_{1z}) \\ I_2 = \rho(N_x \cdot L_{2x} + N_y \cdot L_{2y} + N_z \cdot L_{2z}) \\ I_3 = \rho(N_x \cdot L_{3x} + N_y \cdot L_{3y} + N_z \cdot L_{3z}) \\ \dots \\ I_8 = \rho(N_x \cdot L_{8x} + N_y \cdot L_{8y} + N_z \cdot L_{8z}) \end{cases} \quad (10)$$

These equations may be solved by the least-square algorithm, and the normal vector of a pixel point may be calculated by turning the normal vector into a unit vector. Furthermore, all normal vectors on the WPSs may be computed by stepping through each pixel using the same method. The resulting surface normal vectors are shown in Fig. 8 (b), where Fig. 8(a) depicts the original image of the wear particle.

2.3.2. Surface reconstruction

According to the tangent plane theory, the normal vector is perpendicular to its corresponding tangent plane, therefore, it is perpendicular to each line on the tangent plane. As shown in Fig. 9, if $P(x, y, z_{(x,y)})$ and its adjacent point $P(x+1, y, z_{(x+1,y)})$ are assumed on the tangent plane, a tangent vector V_1 through $P(x, y, z_{(x,y)})$ may be obtained, and defined as:

$$V_1 = (x+1, y, z_{(x+1,y)}) - (x, y, z_{(x,y)}) = (1, 0, z_{(x+1,y)} - z_{(x,y)}) \quad (11)$$

From the analysis above, the surface normal vector is perpendicular to the tangent vector V_1 , namely, $N \cdot V_1 = 0$, and the constraint equation in the horizontal direction may be calculated as:

$$N_x + N_z \cdot (z_{(x+1,y)} - z_{(x,y)}) = 0 \quad (12)$$

In the same way, the constraint equation in the vertical direction may be obtained as:

$$N_y + N_z \cdot (z_{(x,y)} - z_{(x+1,y)}) = 0 \quad (13)$$

Considering these pixels with boundary conditions and some unreasonable surface normal vectors, equations (12) and (13) may be revised as follows:

$$-N_x + N_z \cdot (z_{(x-1,y)} - z_{(x,y)}) = 0 \quad (14)$$

$$-N_y + N_z \cdot (z_{(x,y-1)} - z_{(x,y)}) = 0 \quad (15)$$

Therefore, there always exists two constraint equations for a pixel point (x, y) and the height calculation may be divided into the following four conditions:

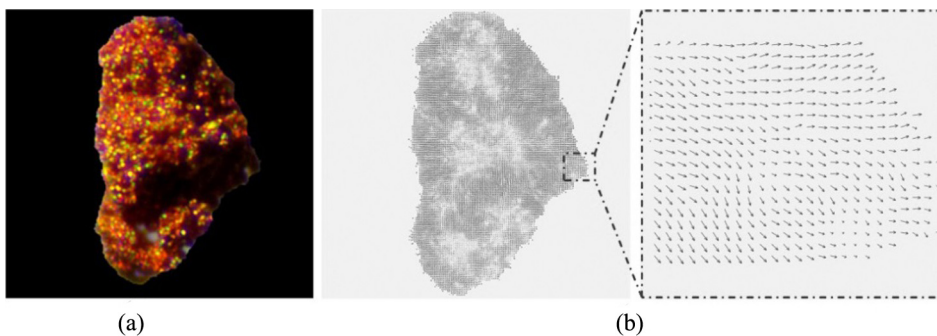


Fig. 8. Normal vector calculation: (a) original wear particle image; (b) 3D surface normal vectors.

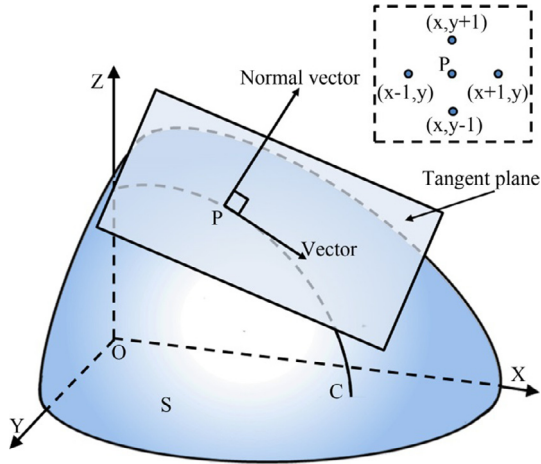


Fig. 9. Schematic diagram of the tangent plane determination.

1. The point (x, y) has valid pixels on both its right and bottom

$$\begin{cases} N_x + N_z \cdot (z_{(x+1,y)} - z_{(x,y)}) = 0 \\ N_y + N_z \cdot (z_{(x,y+1)} - z_{(x,y)}) = 0 \end{cases} \quad (16)$$

2. The point (x, y) has no valid pixel on its right and bottom

$$\begin{cases} -N_x + N_z \cdot (z_{(x-1,y)} - z_{(x,y)}) = 0 \\ -N_y + N_z \cdot (z_{(x,y-1)} - z_{(x,y)}) = 0 \end{cases} \quad (17)$$

3. The point (x, y) has valid pixels on its right and no valid pixel on its bottom

$$\begin{cases} N_x + N_z \cdot (z_{(x+1,y)} - z_{(x,y)}) = 0 \\ -N_y + N_z \cdot (z_{(x,y-1)} - z_{(x,y)}) = 0 \end{cases} \quad (18)$$

4. The point (x, y) has no valid pixel on its right and has valid pixels on its bottom

$$\begin{cases} -N_x + N_z \cdot (z_{(x-1,y)} - z_{(x,y)}) = 0 \\ N_y + N_z \cdot (z_{(x,y+1)} - z_{(x,y)}) = 0 \end{cases} \quad (19)$$

Thus, for an image with $m \times n$ pixels, the surface heights may be calculated by Eq. (20) which consists of a sparse matrix M and a $(2 \times m \times n) \times 1$ vector V .

$$Z = M^{-1}V \quad (20)$$

where M is made up of N_z and V is composed of N_x and N_y .

Fig. 10 depicts a sketch of RWPSs based on the above-mentioned procedures, the surface topographies of wear particles are recovered and reconstructed 3D surfaces are illustrated in Fig. 11. The reconstruction accuracy may be further verified by comparing with the reconstructed surface of the LSCM.

3. Verification of the method

In this section, a set of experiments were performed to verify the performance of the proposed method. First, the MIIs of real particles are collected by the image acquisition system in Section 2, and the 3D surfaces of the wear particles are reconstructed by the proposed method. It further follows that the same wear particles are reconstructed by the LSCM. The reconstruction results from the two methods are shown in Fig. 12. As may be observed, the recovered surfaces by the proposed method exhibit a high similarity with the results by the LSCM. Even though the LSCM is able to reconstruct more fine features than the proposed method, its price is of the magnitude of tens of times as opposed to the traditional confocal microscope. This confocal microscope has always been a great financial burden for general enterprises. Remarkably, this proposed methodology may be able to reconstruct WPSs by optical microscope for reducing the uncertainty of wear particle identification in WDA [28].

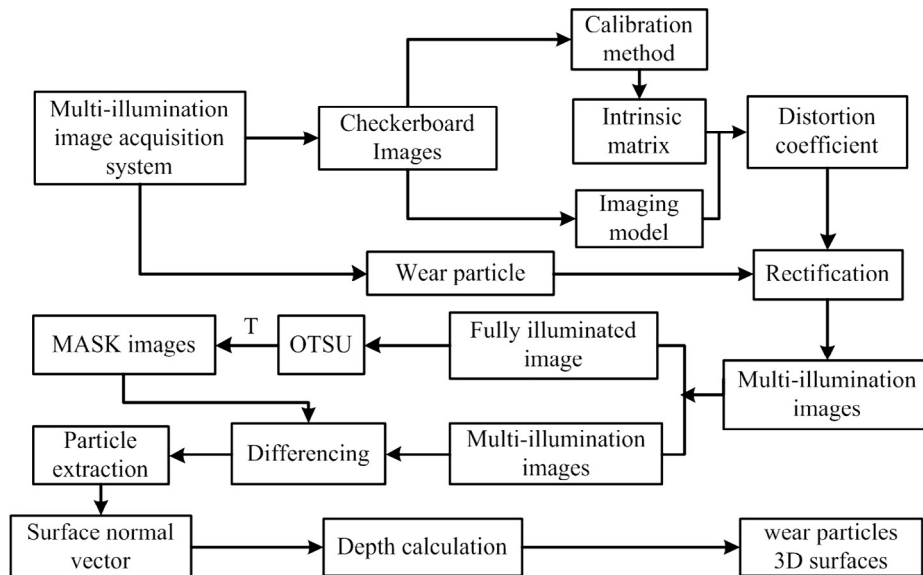


Fig. 10. Flowchart of a WPS reconstruction process.

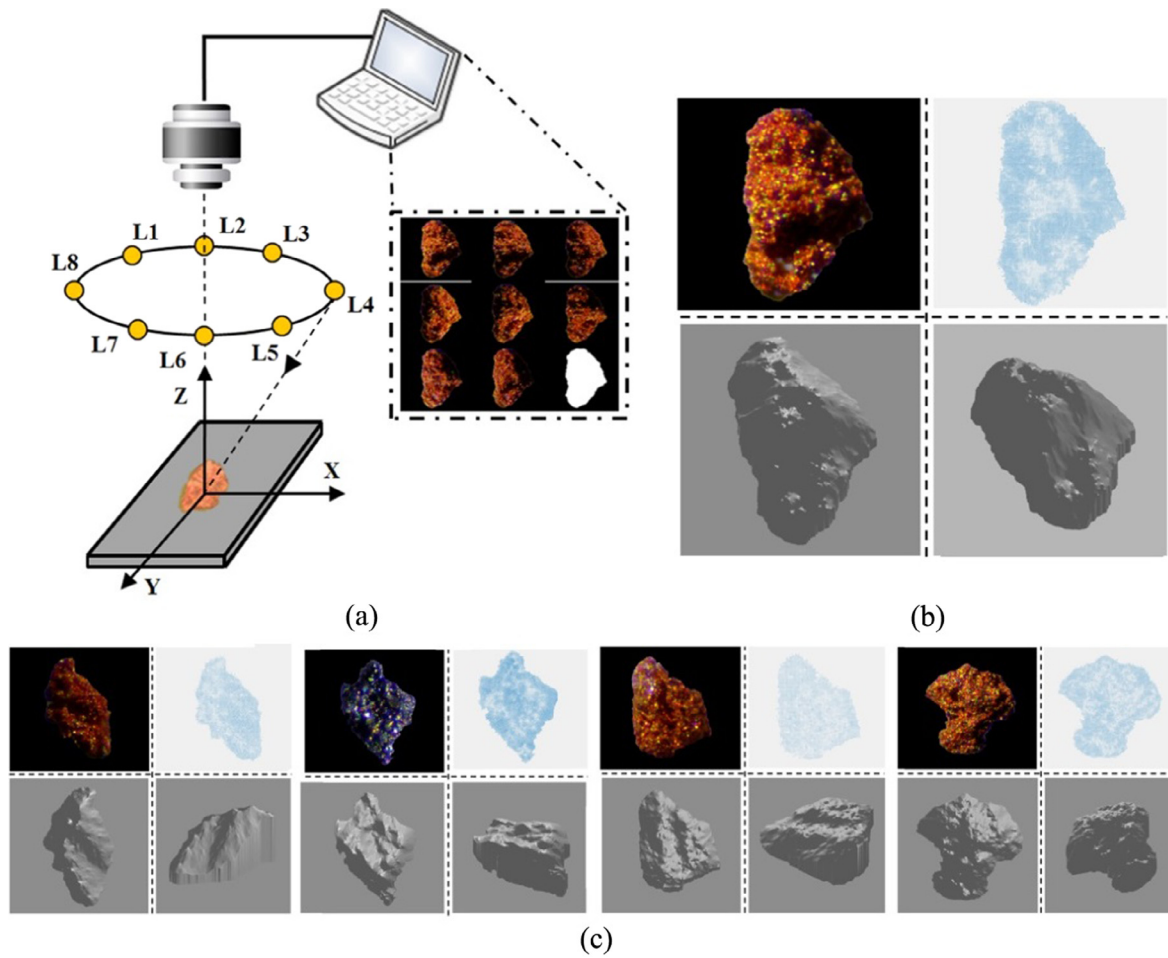


Fig. 11. Wear particle 3D surfaces reconstructed by PS: (a) multi-source particle image acquisition system; (b) amplification of the reconstruction result; (c) reconstruction results of different wear particles.

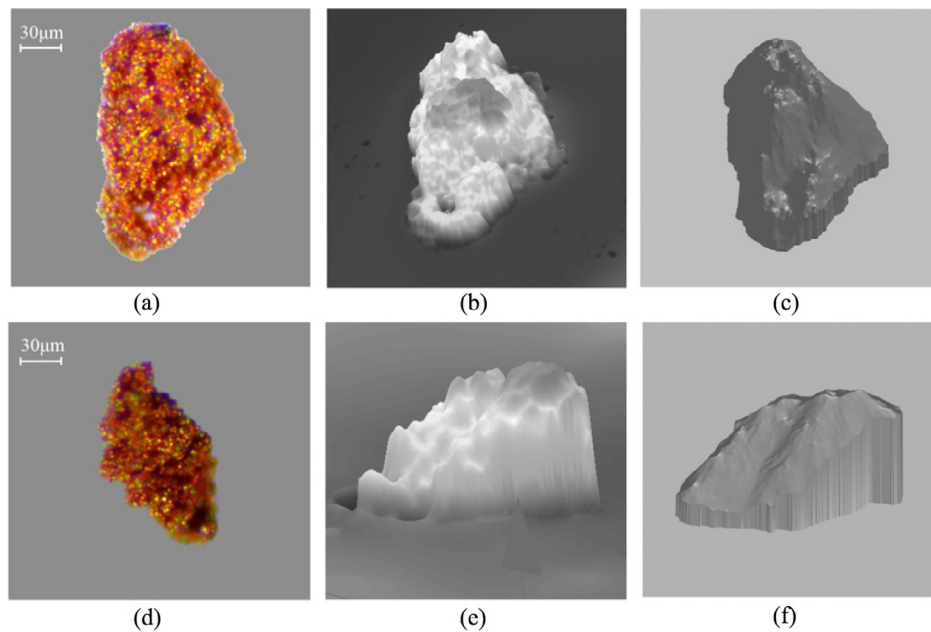


Fig. 12. Comparison of reconstructed WPS: (a) the wear particle 2D image; (b) the reconstructed surface of the wear particle in (a) by the LSCM; (c) the reconstructed surface of the wear particle in (a) by PS; (d) the wear particles 2D image; (e) the reconstructed surface of the wear particle in (d) by the LSCM; (f) the reconstructed surfaces of the wear particle in (b) by PS.

Table 3

The surface parameters extracted from the reconstructed surfaces in Fig. 11 (b) and (c).

Parameter	PS	LSCM
Ssk	1.18	1.11
Sku	1.47	1.26
Sbi	0.48	0.58
Svi	1.26×10^{-5}	7.14×10^{-5}

In order to evaluate the reconstructed surfaces comprehensively, the parameters of reconstructed surfaces are extracted to make a contrast. According to surface properties, surface parameters may be divided into four categories; the amplitude parameter, the space parameter, the comprehensive parameter, and the function parameter, respectively [11]. Amongst them, the amplitude parameter is able to reflect surface morphology, and the function parameter represents some special performance indicator. Therefore, some typical parameters are selected from the amplitude and from the function parameters, these include the surface skewness (Ssk), the surface kurtosis (Sku), the surface bearing index (Sbi), and the valley fluid retention index (Svi), respectively. These parameters were extracted from the reconstructed surfaces in Fig. 11 (b) and (c), shown in Table 3.

As may be observed, the four parameters are approximately the same which is a good reflection of the similarity of reconstructed results on the surface morphology. Overall, the wear particle reconstruction based on the PS has a high similarity to the results exhibited by the LSCM.

4. Discussion

Through the design of an image acquisition device with a microscope and eight LEDs, MILs are captured from a fixed view, and WPSs are reconstructed by the PS method. The above experiments clearly confirm that the developed photometric-stereo based method is able to reconstruct the 3D surface of wear particles with a good accuracy. In comparison to the traditional ferrography described in the introduction section, this developed method may provide the 3D surface morphologies. With an optical microscope, the surface of the wear particle is reconstructed at a very low-cost means than the LSCM approaches. When compared with the multi-view image capturing system reported in the reference [18], the current work provides surface features rather than spatial features, such as valley fluid retention index (Svi). More significantly, this proposed method makes the extracted 3D surface information more reliable for the identification of the wear debris.

It may be mentioned here that the wear debris images must be captured from a fixed view. When collecting MILs, the movement of wear particles will lead to the misplacement of pixel points in collected images, affecting the calculation of the surface normal vectors. Thus, the deposition of the wear particles is one of the key points to obtain these MILs. Therefore, the proposed method could be combined with ferrography to enhance the attraction of wear debris on a plane surface by its magnetic force. The further development of this work has extended the traditional ferrography technology into 3D WDA by reconstructing the wear particle 3D surfaces.

5. Conclusions

The authors have presented a photometric-stereo based system for 3D RWPSs from 2D MILs. The main objective of this method was to improve the performance of the ferrography technology by offering 3D surface information on wear particles. The main system features are: (1) the corrected MIL collection with the designed

device, (2) the wear particle extraction for efficiency improvement, and (3) the 3D s RWPSs from MILs based on photometric stereo. From the comparison of the results, it may be observed that the reconstructed surfaces of the proposed method have a high similarity with the results of the LSCM and the effectiveness of the proposed method has been verified.

Acknowledgements

This work is funded by the National Science Foundation of China (No. 51675403) and through the International Collaborative Plan of Shaanxi province (No. 2017kw-034). Meanwhile, the author gratefully acknowledges the support of K. C. Wang Education Foundation.

References

- [1] M. Niemczewska-Wójcik, Wear mechanisms and surface topography of artificial hip joint components at the subsequent stages of tribological tests, *Measurement* 107 (2017) 89–98.
- [2] S. Wang, T.H. Wu, H.K. Wu, N. Kwok, Modeling wear state evolution using real time wear debris features, *Tribol. Trans.* 60 (6) (2017) 1022–1032.
- [3] J.S. Luo, D.J. Yu, M. Liang, Enhancement of oil particle sensor capability via resonance-based signal decomposition and fractional calculus, *Measurement* 76 (2015) 240–254.
- [4] W. Hong, S. Wang, H. Liu, et al., A hybrid method based on Band Pass Filter and Correlation Algorithm to improve debris sensor capacity, *Mech. Syst. Signal Process* 82 (14) (2017) 1–12.
- [5] B.J. Roylance, Ferrography then and now, *Tribol. Int.* 38 (10) (2005) 857–862.
- [6] J.Q. Wang, J. Bi, L.J. Wang, X.L. Wang, A non-reference evaluation method for edge detection of wear particles in ferrograph images, *Mech. Syst. Signal Process* 100 (2018) 863–876.
- [7] S. Raadnui, Wear particle analysis — utilization of quantitative computer image analysis: a review, *Tribol. Int.* 38 (10) (2005) 871–878.
- [8] T.H. Wu, J.Q. Wang, J.Y. Wu, Y.B. Xie, J.H. Mao, Wear characterization by an on-line ferrograph image, *Proc. IMechE Part J: J. Eng. Tribol.* 225 (2011) 23–34.
- [9] W. Yuan, K.S. Chin, M. Hua, G. Dong, C. Wang, Shape classification of wear particles by image boundary analysis using machine learning algorithms, *Mech. Syst. Signal Process* 72–73 (2016) 346–358.
- [10] M.L. Wang, Z. Peng, Investigation of the nano-mechanical properties and surface topographies of wear particles and human knee cartilages, *Wear* 324–325 (2015) 74–79.
- [11] J.P. Wu, Z. Peng, Investigation of the geometries and surface topographies of UHMWPE wear particles, *Tribol. Int.* 66 (66) (2013) 208–218.
- [12] M.L. Wang, Z. Peng, Investigation of the nano-mechanical properties and surface topographies of wear particles and human knee cartilages, *Wear* 324–325 (324) (2015) 74–79.
- [13] Y. Tian, J. Wang, Z. Peng, X. Jaing, A new approach to numerical characterisation of wear particle surfaces in three-dimensions for wear study, *Wear* 282–283 (8) (2012) 59–68.
- [14] G.P. Stachowiak, G.W. Stachowiak, P. Podsiadlo, Automated classification of wear particles based on their surface texture and shape features, *Tribol. Int.* 41 (1) (2008) 34–43.
- [15] Y.P. Peng, T.H. Wu, S. Wang, N. Kwok, Z. Peng, Motion blurred particle image restoration for on-line wear monitoring, *Sensors* 15 (4) (2015) 8173–8191.
- [16] M.R. Dan, Multi-view and three-dimensional (3D) images in wear debris analysis (WDA), University of Manchester, 2013.
- [17] Y.P. Peng, T.H. Wu, S. Wang, Z. Peng, Oxidation wear monitoring based on the color extraction of on-line wear debris, *Wear* 332 (2015) 1151–1157.
- [18] H.K. Wu, N. Kwok, S.C. Liu, T.H. Wu, Z. Peng, A prototype of on-line extraction and three-dimensional characterisation of wear particle features from video sequence, *Wear* 368–369 (2016) 314–325.
- [19] R.J. Woodham, Photometric method for determining surface orientation from multiple images, *Opt. Eng.* 19 (1) (1980) 139–144.
- [20] L. Xie, Z. Song, G. Jiao, X. Huang, K. Jia, A practical means for calibrating an LED-based photometric stereo system, *Opt. Lasers Eng.* 64 (2015) 42–50.
- [21] K. Hara, K. Nishino, K. Ikeuchi, Light source position and reflectance estimation from a single view without the distant illumination assumption, *IEEE Trans. Pattern Anal. Mach. Intell.* 27 (4) (2005) 493–505.
- [22] Z.Y. Zhang, Flexible camera calibration by viewing a plane from unknown orientations, *Proc. IEEE Int. Conf. Comput. Vision* 1 (1999) 666–673.
- [23] R. Hartley, A. Zisserman, *Multiple View Geometry in Computer Vision*, Cambridge University Press, 2003.
- [24] C.G. Harris, M. Stephens, A Combined Corner and Edge Detector, in: *Proceedings of the 4th Alvey Vision Conference*, Manchester, UK, 1998, pp. 147–151.
- [25] N. Otsu, A threshold selection method from gray level histograms, *IEEE Trans. SMC* 9 (1) (1979) 62–69.
- [26] S.K. Zhou, G. Aggarwal, R. Chellappa, D.W. Jacobs, Appearance characterization of linear Lambertian objects, generalized photometric stereo, and

- illumination-invariant face recognition, *IEEE Trans. Pattern Anal. Machine Intell.* 29 (2) (2007) 230–245.
- [27] Z. Song, R.C. Chung, Real-time three-dimensional fingerprint acquisition via a new photometric stereo means, *Opt. Eng.* 52 (10) (2013) 103103.
- [28] A. Wójcik, P. Klapa, B. Mitka, J. Śladek, The use of the photogrammetric method for measurement of the repose angle of granular materials, *Measurement* 115 (2018) 19–26.
- [29] T. Ridler, S. Calvard, Picture thresholding using an iterative selection method, *IEEE Trans. Syst. Man Cybernet.* 8 (8) (1978) 630–632.
- [30] J.N. Kapur, P.K. Sahoo, A.K.C. Wong, A new method for gray-level picture thresholding using the entropy of the histogram, *Comput. Vision Graph. Image Press.* 29 (3) (1985) 237–285.
- [31] P. Sahoo, C. Wilkins, J. Yeager, Threshold selection using Renyi's entropy, *Pattern Recogn.* 30 (1) (1997) 71–84.